Defense Technical Information Center
Compilation Part Notice

ADP014115

TITLE: Advances in High-Resolution Schemes for Computational Acoustics on General Geometries

DISTRIBUTION: Approved for public release, distribution unlimited Availability: Hard copy only.

This paper is part of the following report:

TITLE: Aging Mechanisms and Control. Symposium Part A - Developments in Computational Aero- and Hydro-Acoustics. Symposium Part B - Monitoring and Management of Gas Turbine Fleets for Extended Life and Reduced Costs [Les mecanismes vieillissants et le controle] [Symposium Partie A - Developpements dans le domaine de l'aeroacoustique et l'hydroacoustique numeriques] [Symposium Partie B ...

To order the complete compilation report, use: ADA415749

The component part is provided here to allow users access to individually authored sections of proceedings, annals, symposia, etc. However, the component should be considered within the context of the overall compilation report and not as a stand-alone technical report.

The following component part numbers comprise the compilation report:
ADP014092 thru ADP014141

Advances in High-Resolution Schemes for Computational Acoustics on General Geometries

Miguel R. Visbal
Computational Sciences Branch
Air Vehicles Directorate
Air Force Research Laboratory
Wright-Patterson AFB, OH 45433
USA

ABSTRACT

A high-order compact-differencing and Pade-type filtering algorithm, coupled with either the standard fourth-order Runge-Kutta scheme or with a sub-iterative implicit method is developed and implemented to simulate aeroacoustic phenomena on curvilinear geometries. Several issues pertinent to the use of such schemes are addressed. The impact of mesh stretching in the generation of high-frequency spurious modes is examined and the need for a discriminating higher-order spatial filter procedure is established and resolved. The incorporation of these filtering techniques also permits a robust treatment of outflow radiation condition by taking advantage of energy transfer to high frequencies caused by rapid mesh stretching. Computations demonstrate that these algorithmic components are also suitable for interface treatments created in domain-decomposition strategies. For three-dimensional computations, special metric relations are employed to assure the fidelity of the scheme in curvilinear and dynamic meshes. Application to several benchmark 2D and 3D problems demonstrates the success of the overall computational approach.

INTRODUCTION

An important aspect of both civilian and military aircraft operation is the impact of aerodynamically generated sound on communities and structures. Examples of applications of current interest include weapon cavity acoustics, jet screech, sonic boom, cabin noise, and sound generated by blade/vortex interactions. The relatively new field of time-domain computational aeroacoustics (CAA) focuses on the accurate prediction of aerodynamic sound generated by airframe components and propulsion systems, as well as on its propagation and far-field characteristics. Both aspects of the problem (*i.e.* sound generation and propagation) are extremely demanding from a time-domain computational standpoint due to the large number of grid points and small time-steps that are typically required. Therefore, for realistic aeroacoustic simulations to become more feasible, higher-order accurate and optimized numerical schemes are sought in order to reduce the required number of grid points per wavelength while still ensuring tolerable levels of numerically-induced dissipation and dispersion. These strict simulation requirements are shared by other time-domain wave propagation applications such as computational electromagnetics.

Recent reviews of computational aeroacoustics have been given by Tam[1] and Wells and Renaut[2] who discuss various numerical schemes currently popular in CAA. These include among others the dispersion-relation-preserving (DRP) scheme of Tam and Webb[3], the family of high-order compact differencing schemes of Lele[4] and Essentially Non-Oscillatory (ENO) schemes[5]. The DRP and compact schemes are centered non-dissipative schemes, a property which is desirable for linear wave propagation. However, their inherent lack of numerical dissipation results in spurious numerical oscillations and instability in practical applications involving general geometries, approximate boundary conditions or non-linear features. In the DRP approach for instance, artificial selective damping must be employed under these conditions[1]. While quite robust, standard upwind and upwind-biased formulations are undesirable for situations involving linear wave propagation due to their excessive dissipation. To overcome this difficulty, higher-order upwind or ENO approaches must be employed. The above spatial semi-discretizations are typically combined with high-order explicit time-integration methods such as the multi-stage Runge-Kutta procedure. In addition to the spatial and temporal discretizations, another critical aspect in CAA simulations is the accurate treatment of the physical and computational boundary conditions. A recent review of radiation, outflow and wall boundary treatments has been provided in Ref. 6.

This paper focuses on the development and evaluation of a high-order computational methodology for aeroacoustic simulation on general geometries. There are two primary components to the algorithm chosen in the present work. The

first is the spatial differencing scheme, for which the choice rests primarily on Padc-typc tridiagonal-based fourth- and sixth-order compact-difference formulas[4]. As compared to explicit schemes, this approach incurs an increase in computational cost but lowers the dispersion error and reduces the number of points near the boundary where special formulations are required. As noted earlier, the non-dissipative nature of centered schemes makes them susceptible to the unrestricted growth of spurious perturbations. This issue is resolved through the incorporation of high-order spatial low-pass filters. The filters are based on Pade-type formulas requiring the solution of tridiagonal systems of equations. The expressions are taken from Ref. 7, where up to 10th-order filters were employed to stabilize finite-volume electromagnetics calculations, and have been successfully extended to solve the Navier-Stokes equations[8]. Time integration is achieved through the use of a either the standard 4th-order Runge-Kutta algorithm or an implicit sub-iterative third-order method. The solver is written in general curvilinear coordinates in order to handle non-trivial geometries. The various components of the numerical procedure are described below with particular emphasis on metric evaluation for 3-D and dynamic meshes, multi-domain interface treatment and the extension of the filtering scheme to treat outflow radiation boundaries. The accuracy properties of the scheme, and the efficacy of the high-order low-pass filter approach, are highlighted by considering several benchmark test-cases on single and multiple domains.

METHODOLOGY

GOVERNING EQUATIONS
In order to develop a procedure suitable for nonlinear fluid dynamic, aeroacoustic and aeroelastic applications over complex configurations, the full Navier-Stokes equations are selected and are cast in strong conservative form introducing a general time-dependent curvilinear coordinate transformation $(x,y,z,t) \rightarrow (\xi, \eta, \zeta, \tau)$. In vector notation, and employing non-dimensional variables, these equations can be written as:

$$\partial(\bar{U}/J)/\partial\tau + \partial\hat{F}/\partial\xi + \partial\hat{G}/\partial\eta + \partial\hat{H}/\partial\zeta = (1/\text{Re})[\partial\hat{F}v/\partial\xi + \partial\hat{G}v/\partial\eta + \partial\hat{H}v/\partial\zeta] + \bar{S}/J \qquad (1)$$

where F, G, H, F_v, G_v, H_v are the fluxes, S denotes an imposed acoustic source, and J is the coordinate transformation Jacobian, which for dynamic meshes, is also a function of time. The specific form the fluxes appearing in Eq. (1) can be found for instance in Ref. 9.

SPATIAL DISCRETIZATION
A finite-difference approach is employed to discretize the above equations. This choice is motivated by the relative ease of formal extension to higher-order accuracy. For any scalar quantity, ϕ, such as a metric, flux component or flow variable, the spatial derivative ϕ' is obtained in the transformed plane by solving the tridiagonal system:

$$\Gamma\phi'_{i-1} + \phi'_i + \Gamma\phi'_{i+1} = b\frac{\phi_{i+2}-\phi_{i-2}}{4} + a\frac{\phi_{i+1}-\phi_{i-1}}{2} \qquad (2)$$

where Γ, a and b determine the spatial properties of the algorithm. The formula yields the compact five-point, sixth-order (C6) and three-point fourth-order (C4) schemes with $\Gamma=1/3$, $a=14/9$, $b=1/9$ and $\Gamma=1/4$, $a=3/2$, $b=0$ respectively. Equation (2) also incorporates the standard explicit fourth-order (E4) and second-order (E2) approaches for which the coefficients are ($\Gamma=0$, $a=4/3$, $b=-1/3$) and ($\Gamma=0$, $a=1$, $b=0$) respectively. The dispersion characteristics and truncation error of the above schemes can be found in Refs. 4 and 10. It should be noted that for a given order of accuracy, the compact schemes are significantly superior to their explicit (non-compact) counterparts.

FILTERING SCHEME
Compact-difference discretizations, like other centered schemes, are non-dissipative, and therefore susceptible to numerical instabilities due to the unrestricted growth of high-frequency modes. These difficulties originate from several sources including mesh non-uniformity, approximate boundary conditions and nonlinear flow features. In order to extend the present solver to practical simulations, while retaining the improved accuracy of the spatial compact discretization, a high-order implicit filtering technique [7,8] is incorporated. If a typical component of the solution vector is denoted by ϕ, filtered values $\bar{\phi}$ satisfy,

$$\alpha_f\bar{\phi}_{i-1} + \bar{\phi}_i + \alpha_f\bar{\phi}_{i+1} = \sum_{n=0}^{N}\frac{a_n}{2}(\phi_{i+n} + \phi_{i-n}) \qquad (3)$$

Equation (3) is based on templates proposed in Ref. 4 and with proper choice of coefficients, provides a 2Nth-order formula on a 2N+1 point stencil. The N+1 coefficients, a_o, a_1, ..., a_N, are derived in terms of α_f with Taylor- and Fourier-series analyses and are found in Refs. 8, 10 and 11, along with the corresponding spectral filter responses. The adjustable parameter α_f satisfies the inequality $-0.5 < \alpha_f < 0.5$, with higher values of α_f corresponding to a less

dissipative filter. In multi-dimensional problems, the filter operator is applied sequentially in each coordinate direction. The specified interior filter formula is denoted by appending its designation to that of the scheme. For example, *C6F10* designates the sixth-order compact scheme combined with a tenth-order filter. For the near-boundary points, the filtering strategies described in Refs. 8 and 11 are employed.

METRIC EVALUATION

The extension of high-order schemes to non-trivial 3-D geometries demands that issues of freestream preservation and metric cancellation be carefully addressed. These errors, which arise in finite-difference discretizations of governing equations written in strong-conservation form, can catastrophically degrade the fidelity of standard second-order as well as higher-order approaches[8,12]. In deriving the flow equations in strong-conservation form, the following metric identities have been implicitly invoked,

$$I_1 = (\xi_x/J)_\xi + (\eta_x/J)_\eta + (\zeta_x/J)_\zeta = 0$$

$$I_2 = (\xi_y/J)_\xi + (\eta_y/J)_\eta + (\zeta_y/J)_\zeta = 0 \tag{4}$$

$$I_3 = (\xi_z/J)_\xi + (\eta_z/J)_\eta + (\zeta_z/J)_\zeta = 0$$

$$I_4 = (1/J)_\tau + (\xi_t/J)_\xi + (\eta_t/J)_\eta + (\zeta_t/J)_\zeta = 0$$

In Ref. 8 it was shown that on highly distorted (static) curvilinear 2-D meshes, the compact scheme exhibits freestream preservation when the metrics are evaluated with the same finite-difference expressions as those employed for the fluxes. It was also demonstrated that the practice of prescribing *analytic* metrics on stretched curvilinear grids can lead to unacceptable errors and therefore should in general be avoided. The previous straightforward approach of calculating the metrics, although effective in 2-D, fails to provide metric cancellation for general 3-D curvilinear configurations. To illustrate this point, consider the standard metric relations:

$$\xi_x/J = y_\eta z_\zeta - y_\zeta z_\eta$$
$$\eta_x/J = y_\zeta z_\xi - y_\xi z_\zeta \tag{5}$$
$$\zeta_x/J = y_\xi z_\eta - y_\eta z_\xi$$

associated with the identity I_1. Evaluation of the y and z derivatives in the previous expressions using explicit or compact centered schemes does not satisfy I_1, and as a result, significant grid-induced errors may appear[12,13]. In order to extend the high-order compact scheme to general geometries, the metric terms are rewritten prior to discretization in the equivalent (conservative) form[14]:

$$\xi_x/J = (y_\eta z)_\zeta - (y_\zeta z)_\eta$$
$$\eta_x/J = (y_\zeta z)_\xi - (y_\xi z)_\zeta \tag{6}$$
$$\zeta_x/J = (y_\xi z)_\eta - (y_\eta z)_\xi$$

Similar expressions are employed for the remaining metric terms in order to satisfy the identities I_2 and I_3 above. When the transformation metrics are recast in this manner, and the derivatives are evaluated with the same high-order formulas employed for the fluxes, freestream preservation is again recovered in general time-invariant 3-D curvilinear geometries[12].

For deforming and moving meshes, the identity I_4 must be also satisfied to eliminate metric cancellation errors and to ensure freestream preservation. This metric identity is referred to in the literature[14] as the Geometric Conservation Law (*GCL*). For the time-integration methods employed in this work, the time-derivative term in Eq. (1) is split using chain-rule differentiation as follows:

$$(\vec{U}/J)_\tau = (1/J)\vec{U}_\tau + \vec{U}(1/J)_\tau \tag{7}$$

Rather than attempting to compute the time derivative of the inverse Jacobian directly from the grid coordinates at various time levels (either analytically or numerically), we simply invoke the *GCL* identity I_4 to evaluate $(1/J)_\tau$, i.e.

$$(1/J)_\tau = -[(\xi_t/J)_\xi + (\eta_t/J)_\eta + (\zeta_t/J)_\zeta] \tag{8}$$

where

$$\xi_t/J = -[x_\tau(\xi_x/J) + y_\tau(\xi_y/J) + z_\tau(\xi_z/J)]$$
$$\eta_t/J = -[x_\tau(\eta_x/J) + y_\tau(\eta_y/J) + z_\tau(\eta_z/J)] \tag{9}$$
$$\zeta_t/J = -[x_\tau(\zeta_x/J) + y_\tau(\zeta_y/J) + z_\tau(\zeta_z/J)]$$

For the case of an analytically prescribed dynamic mesh transformation, the grid speeds (x_τ, y_τ, z_τ) are obtained from the corresponding analytic expressions. An example in which the grid speeds are known analytically corresponds to the

case of a maneuvering wing when the entire mesh is rotated in a rigid fashion. In many practical applications involving deforming meshes (*e.g.* dynamic aeroelastic simulations), the grid speeds are not known *a priori*, and must therefore be approximated to the desired degree of accuracy employing the evolving grid coordinates at several time levels. As demonstrated in Ref. 15, the high-order method retains its superior accuracy on rapidly distorting meshes when the procedure outlined above is incorporated for the time metrics.

TIME-INTEGRATION SCHEME

Two different time-integration approaches are incorporated in the present family of solvers. For wave propagation applications, the equations are integrated in time with the classical fourth-order four-stage Runge-Kutta method (*RK4*). The scheme is implemented in low storage form requiring three levels of storage. For highly stretched grids exhibiting very small volumes, the stability constraint of the explicit time-marching scheme is found to render the approach too restrictive and inefficient. Therefore, the implicit, approximately-factored method of Beam and Warming[16] is also incorporated and augmented through the use of Newton-like subiterations in order to achieve high-order time accuracy. In delta form, the second-order form of the scheme (denoted as *BW2*) may be written as:

$$\left[I + \left(\frac{2\Delta t}{3}\right)\delta_\xi\left(\frac{\partial F^p}{\partial Q} - \frac{1}{Re}\frac{\partial F_v^p}{\partial Q}\right)\right] \times \left[I + \left(\frac{2\Delta t}{3}\right)\delta_\eta\left(\frac{\partial G^p}{\partial Q} - \frac{1}{Re}\frac{\partial G_v^p}{\partial Q}\right)\right] \times \left[I + \left(\frac{2\Delta t}{3}\right)\delta_\zeta\left(\frac{\partial H^p}{\partial Q} - \frac{1}{Re}\frac{\partial H_v^p}{\partial Q}\right)\right]\Delta Q$$

$$= -\left(\frac{2\Delta t}{3}\right)\left[\left(\frac{1}{2\Delta t}\right)\left(3Q^p - 4Q^n + Q^{n-1}\right) + \delta_\xi\left(F^p - \frac{1}{Re}F_v^p\right) + \delta_\eta\left(G^p - \frac{1}{Re}G_v^p\right) + \delta_\zeta\left(H^p - \frac{1}{Re}H_v^p\right) + S^p\right]$$

(10)

The spatial derivatives in the implicit operators are represented using standard second-order centered approximations whereas high-order discretizations are employed for the explicit side. Nonlinear artificial dissipation terms[17] are also appended to the implicit operator to enhance stability. In addition, for improved efficiency, the approximately-factored scheme is recast in diagonalized form[18]. Any degradation in solution accuracy caused by the spatial second-order implicit operators, artificial dissipation and the diagonal form is eliminated through the use of sub-iterations (typically, three sub-iterations are used per time step). By changing the number of time levels employed to evaluate the time-derivative term appearing in the *RHS* of Eq. (10), first (*BW1*) and third (*BW3*) order accurate forms of the implicit algorithm can be constructed.

MULTI-DOMAIN STRATEGY

Domain-decomposition techniques constitute an important component of modern computational strategy. Due to their spatially implicit nature, Pade-type schemes are more difficult to utilize in a multi-domain environment than explicit methods. However, a finite-size overlap can be employed with the present compact/filtering methodology to generate a powerful approach applicable to complicated curvilinear meshes[11,12]. Figure 1 depicts schematically the case of a simulation employing two sub-domains. The original domain of computation is divided into two parts to be distributed to different processors. Each sub-domain is supplemented with several points from the adjacent sub-domain to form an overlap region, whose details for a five-point vertical overlap are also shown in Fig. 1. Although the overlap points are collocated, they have been shown slightly staggered for clarity. Each vertical line is denoted by its *i*-index. Data is exchanged between adjacent sub-domains at the end of each sub-iteration of the implicit scheme (or each stage of *RK4*), as well as after each application of the filter. The values at points *1* and *2* of Mesh 2 are set to be identically equal to the corresponding updated values at points *IL-4* and *IL-3* of Mesh 1. Similarly, reciprocal information is transferred through points *4* and *5* of Mesh 2 which "donate" values to points *IL-1* and *IL* of Mesh 1. More details on the accuracy and robustness of the present multi-domain approach can be found in Ref. 11.

RESULTS

IMPACT OF SPATIAL FILTERING ON STRETCHED MESHES

In practical scattering simulations, grid stretching is usually employed in order to reduce required computational resources, as well as to permit the use of approximate farfield boundary conditions. Therefore, the performance of high-order schemes on general stretched meshes must be carefully examined.

An enlightening analysis of the behavior of a smooth solution as it passes through a sudden mesh coarsening has been presented by Vichnevetsky[19] for the 1-D advection equation semi-discretized with the standard second-order centered scheme. This analysis indicates that although total energy is preserved, at the grid coarsening interface, a significant portion of the energy is deposited on a *reflected* solution composed primarily of odd-even modes and modulated by a smooth envelope. This reflected energy propagates upstream (*i.e.* with negative group velocity) and in most circumstances if left unchecked has the potential of ultimately contaminating the genuine solution. However, since reflections due to grid stretching are characterized by high-frequency modes, they can be easily removed by the

high-order low-pass spatial filter. The effectiveness of the low-pass filter in controlling spurious reflections without degrading the fidelity of the solution was demonstrated previously in Ref. 12.

The combination of grid stretching with a discriminating low-pass filter may be exploited as an alternative procedure for outflow boundary treatment. By employing a large rate of stretching, a significant amount of energy can be reflected at the grid coarsening interfaces. Provided this *reflected* energy is deposited into high-frequency modes (in the fine mesh region), it can then be subsequently eliminated by the baseline low-pass filter without contaminating the genuine solution. Furthermore, the *transmitted* energy is also quickly dissipated by the high-order filter, as the transmitted solution features are represented by a diminishing number of points per wave in the stretching mesh. This proposed method eliminates the need for more sophisticated (and perhaps more restrictive) boundary conditions at the expense of extending the computational domain. Although the proposed approach has a mathematical foundation (at least based on the 1-D analysis of Ref. 19), its implementation is highly empirical, and therefore its utility must be evaluated in the context of practical applications.

As a severe test case, consider the propagation of acoustic waves in the grid of Fig. 2a. This mesh is uniform ($\Delta x = \Delta y = 0.05$) in the center of the computational domain ($-3 < x, y < 3$). Outside of this resolved region, Δx and Δy are increased abruptly. An acoustic source is specified according to the expression

$$S(x,y,t) = exp\{(ln2)\ [(x-x_c)^2+(y-y_c)^2/b^2]\}\ sin(\omega t)\ f(t) \tag{11}$$

$$f(t) = min\{\ 1.0,\ (t/t_o)^3\} $$

with $x_c = y_c = 0$, $\omega = 5\pi$, $b = 0.2$ and $t_o = 4$. A snapshot of the pressure is displayed in Fig. 2b. It is apparent that the acoustic energy reflected at the grid-coarsening interface is almost completely annihilated by the high-order filter. The corresponding plot of the instantaneous pressure along the diagonal ($x = y$) is shown in Fig. 2c and indicates that the transmitted energy diffuses rapidly in the coarse mesh region. For this square grid, the circular waves cross the grid interface at a varying angle of incidence without apparent anisotropies being introduced. More quantitative tests demonstrating the suitability of the present far field radiation treatment can be found in Ref. 13 for a transient acoustic pulse and a convective vortical disturbance.

SCATTERING OF AN ACOUSTIC PULSE

In order to validate the present approach for curvilinear geometries, we select as a test case the benchmark problem denoted as Category I, Problem 2 in the 2nd CAA Workshop of Ref. 20. This configuration (Fig. 3) describes the scattering off a circular cylinder of a prescribed initial pressure pulse. The pulse at $t = 0$ is given by the expression

$$p = p_o + \varepsilon\ exp\{(ln2)\ [(x-x_c)^2+(y-y_c)^2/b^2]\} \tag{12}$$

with $x_c = 4$, $y_c = 0$, $\varepsilon = 0.01$, $b = 0.2$.

Along the cylinder surface, standard inviscid wall boundary conditions are employed. Since the configuration is symmetric, only the upper half of the domain is considered, and symmetry conditions are invoked along $\theta = 0^o$, 180°. As indicated in Fig. 3a, the grid is stretched for $r/D > 7$ using a constant stretching factor of 1.1. Since in this coarse-mesh region the outgoing pulse is dissipated by the baseline filter, a simple extrapolation condition is suitable along the far field boundary. A polar-type grid of size 156X175 is employed, and the solution is advanced in time with a non-dimensional time step $\Delta t = 0.004$.

Pressure contours depicting pulse propagation and reflection off the cylinder surface are shown in Fig. 3 at several instants in time for the *C6F10-RK4* scheme. The history of the pressure at a selected point ($r/D=5$, $\theta=90^o$) and for several computations is presented in Fig. 4. On this relatively coarse mesh, the *C6F10-RK4* and *C4F8-RK4* schemes with a filter coefficient $\alpha_f = 0.4$ are observed to be in good agreement with the exact solution[20]. However, on this mesh, the *C4* scheme combined with an 8th-order *explicit* filter (*i.e.* $\alpha_f = 0$) displays appreciable error. This highlights the improved accuracy of the implicit filter formulation.

Results computed using the implicit sub-iterative time-marching scheme are provided in Fig. 5. These results were obtained with a non-dimensional time step $\Delta t = 0.004$ and employing two sub-iterations. The first order time advancement method (*BW1*) is found to be highly dissipative. However, significant improvement is achieved by

employing the second-order implicit approach (*BW2*). Finally, the third-order iterative implicit method (*BW3*) is in very close agreement with the fourth-order explicit (*RK4*) solution (see figure inset).

In order to demonstrate the advantages of the implicit time-marching scheme, we consider the previous pulse scattering example for the case of an elliptic cylinder of aspect ratio 10 (Fig. 6). As Fig. 6a indicates, the grid is highly clustered near the small radius of curvature at the edge of the ellipse. This results in small grid cells and consequently in a significant reduction of the allowable time step for the explicit method. Calculations employing the *RK4* scheme were found to be unstable even for a non-dimensional time step as low as $\Delta t = 0.000125$ which correspond to a maximum *CFL* number of approximately 0.96. Therefore it becomes apparent that the explicit time-marching method is very inefficient for general geometries wherein highly clustered meshes are necessary (*e.g.* sharp edges). By contrast, the third-order implicit iterative scheme was found to remain stable for the baseline time step ($\Delta t = 0.004$) which corresponds to $CFL_{max} \sim 31$. The corresponding instantaneous pressure contours obtained with the implicit method at $t = 1.5$ are displayed in Fig. 6b.

MULTI-DOMAIN SCATTERING SIMULATION

This case corresponds to Category I, Problem 1 in Ref. 20, and considers the scattering from a circular cylinder of a periodic acoustic source (Fig. 7a). This example constitutes a more stringent test of the algorithm and boundary conditions since an asymptotic periodic solution must be attained, and long-term numerical stability demonstrated. In addition, in order to highlight the capability of the present numerical approach to treat a multiple-domain situation, the single-domain grid, consisting of 361 X 321 points, is split along $\theta = 90^\circ$, where extra ξ-lines are added to form a five-point overlap as in Fig. 1. Solutions are advanced separately on each sub-domain, and information is exchanged at the overlap points in the manner previously discussed. The *C6* scheme is employed for interior points along with fourth- and fifth-order compact operators at the boundary and next-to-boundary points respectively whereas *RK4* is utilized for time-integration. In the interior of each sub-domain, a 10th-order filter is utilized whereas high-order one-sided techniques, are invoked near boundaries. For all filter operators, the coefficient $\alpha_f = 0.45$ is specified.

Figure 7b displays instantaneous pressure contours in the vicinity of the cylinder. It is apparent that the pressure waves cross the grid interface without producing any noticeable disruptions of the interference pattern even though pressure waves generated by the source propagate through the overlap region in an oblique direction to the zonal interface. A quantitative comparison of the single-domain, multiple-domain and analytic solutions is given in Fig. 7c in terms of the directivity of the radiated sound at $r/D = 5$. The directivity obtained with a 6th-order near-boundary filter in the overlap region is essentially the same as the corresponding single-domain baseline solution, and both results are in excellent agreement with the theoretical solution. These results highlight the potential of the present high-order methodology for domain-decomposition applications on parallel computers.

ACOUSTIC PROPAGATION ON 3-D CURVILINEAR MESHES

This validation case considers the propagation of a 3-D spherical pulse in a curvilinear mesh in order to examine metric cancellation errors. A three-dimensional curvilinear 61X61X61 mesh is generated using the equations given in Ref. 13, providing a grid in which the metric identities (Eq. (4)) are not trivially satisfied. A constant ζ-plane of the mesh at the location of maximum deformation is shown in Fig. 8a. The imposed grid undulations are resolved with approximately 15 points per wave. An initial pressure pulse is prescribed by

$$p = po + \varepsilon\, exp\{ (-ln2)\ (x^2 + y^2 + z^2)\, /\, 9\}$$

where $\varepsilon = 0.01$.

The pulse propagation problem is computed with a $\Delta t = 0.004$ using the *C4F10-RK4* algorithm with $\alpha_f = 0.49$. Figure 8b displays the calculated pressure contours on a plane through the center of the spherical pulse at $t=10$ for the case when the metrics are evaluated in the standard fashion of Eq. (5). It is apparent that significant distortion of the wave front occurs due to the lack of freestream preservation (*i.e.* metric cancellation errors). The perturbation pressure along the grid line $i=j=31$, (Fig. 8d) indicates gross departure from the theoretical solution. The results obtained with the metric evaluation procedure of Eq. (6) exhibit no distortions of the spherical front (Fig. 8c) and are in excellent agreement with the exact solution (Fig. 8d). Calculations with *C6F10* (not shown) displayed reduced sensitivity to the choice of metric evaluation procedure. This is in agreement with the results of Ref. 12, wherein metric cancellation errors were shown to decrease with increasing order of accuracy. Nonetheless, without the incorporation of Eq. (6) in the calculation of the metric relations, all solutions on this distorted mesh were found to be of poor quality. Hence, even for relatively benign 3-D curvilinear grids, freestream preservation errors may swamp acoustic pressure levels unless proper metric evaluation procedures are employed. It should be noted that analytic metric evaluation (even if available)

does not remedy the situation [8,12]. The present results clearly demonstrate that the superior performance of the high-order method can be extended to the realm of general curvilinear grids including moving/deforming meshes as highlighted in the fluid/structure interaction described next.

ACOUSTO-STRUCTURAL-FLUID INTERACTION OVER A FLEXIBLE PANEL

As a final example of a simulation of multi-disciplinary physics with the present methodology, consider a transitional boundary-layer flow over a flexible finite panel embedded in a rigid surface as shown schematically in Fig. 9a. This problem is closely related to classic panel flutter phenomena, as well as to viscous flow over compliant surfaces. The panel of length a and thickness h extends over the region $0.5 < x/a < 1.5$. The leading-edge region of the plate ($-0.5 < x/a < 0.0$) is formed by an ellipse of half-thickness $0.05h$ (*i.e.* aspect ratio 10). An additional challenge posed by this aeroelastic simulation is the need to accomodate the surface deflection with a dynamically deforming mesh. The problem has been examined in great detail in Ref. 21, which should be consulted for details regarding boundary condition implementation and mesh resolution studies. For brevity, only select results obtained at a freestream Mach number $M = 0.8$ and $Re_a = 10^5$ are summarized here to highlight the ability of the method to capture the complicated unsteady phenomena under the influence of flow-induced surface deformation. This case was computed employing the *C6F10-BW2* scheme.

At low values of the dynamic pressure, a steady flow is obtained despite the adverse pressure gradient induced by the downward deflection of the panel. At higher dynamic pressures, however, a traveling-wave-flutter phenomenon is observed as summarized in Fig. 9b, c. The instantaneous panel shapes (not shown) display a seventh-mode oscillation with a dominant non-dimensional frequency $St = fa/U = 1.52$ which is substantially higher than the fundamental frequency of the elastic plate. The high-mode flexural deflections are observed to travel along the panel and to reflect at the panel edges. These high-frequency fluctuations result in a pronounced acoustic radiation pattern above the vibrating plate, shown in Fig. 9b in terms of the instantaneous pressure field. Downstream of the flexible surface, a regular train of vortical disturbances is observed (Fig. 9c) with characteristic wavelength and frequency compatible with those of Tollmien-Schlichting (T-S) instability. The traveling wave flutter appeared to originate from the coupling of the T-S waves with the panel high-mode transverse fluctuations, and this convective instability ceases below a critical value of Reynolds number.

SUMMARY

A high-order finite-difference method has been adapted to simulate aeroacoustic phenomena on curvilinear geometries. The scheme is based on 4th- and 6th-order compact differencing formulas coupled with up to 10th-order Pade-type low-pass spatial filters. Both explicit and iterative implicit time-marching schemes are considered. The high-order spatial filtering procedure is required in order to maintain stability in the presence of mesh stretching and approximate boundary conditions while ensuring high fidelity for wave propagation. The incorporation of these filtering techniques also permit a robust treatment of outflow radiation condition by taking advantage of energy transfer to high-frequencies caused by rapid mesh stretching. The potential of the procedure for parallel implementation is demonstrated by successful application to multi-domain scattering cases. Special metric procedures are also shown to be essential in the simulation of acoustic phenomena in general curvilinear three-dimensional meshes.

Acknowledgments

REFERENCES

1. Tam, C.K.W., "Computational Aeroacoustics: Issues and Methods, *AIAA J.*, Vol. 33 No. 10, 1995
2. Wells, V. L. and Renaut, "Computing Aerodynamically Generated Noise", *Annual Review of Fluid Mechanics*, Vol. 29, 1997.
3. Tam, C.K.W. and Webb, J.C., "Dispersion-Relation-Preserving Finite Difference Schemes for Computational Acoustics, *J. Comp. Phys.*, Vol. 107, 1993.
4. Lele, S.K., "Compact Finite Difference Schemes with Spectral-Like Resolution", *J. Comp. Phys.*, Vol 103, No. 1, Nov., 1992.
5. Casper, J., "Using High-Order Accurate Essentially Nonoscillatory Schemes for Aeroacoustic Application", *AIAA J.*, Vol. 34, 1994.
6. Tam, C.K.W., "Advances in Numerical Boundary Conditions for Computational Aeroacoustics", AIAA Paper 97-1774, 1997.
7. Gaitonde, D.V., Shang, J.S. and Young, J.L., "Practical Aspects of Higher-Order Numerical Schemes for Wave Propagation Phenomena", *Int. Jnl. Of Num. Methods in Eng.*, Vol. 45, 1999.
8. Visbal, M. and Gaitonde, D. "High-Order Accurate Methods for Complex Unsteady Subsonic Flows", *AIAA J.*, Vol. 37, No. 10, 1999.
9. Anderson, D., Tannehill, J. and Pletcher, R., *Computational Fluid Dynamics and Heat Transfer*, McGraw-Hill Book Co., 1984.

10. Gaitonde, D. and Visbal, M., "High-Order Schemes for Navier-Stokes Equations: Algorithm and Implementation into FDL3DI", Technical Report AFRL-VA-WP-TR-1998-3060, Air Force Research Lab., Wright-Patterson AFB, 1998.

11. Gaitonde, D. and Visbal, M., "Pade-Type High-Order Boundary Filters for the Navier-Stokes Equations", *AIAA J.*, Vol. 38, No. 11, 2000.

12. Gaitonde. D. and Visbal, M., "Further Development of a Navier-Stokes Solution Procedure Based on Higher-Order Formulas", AIAA Paper 99-0557, 1999.

13. Visbal, M. and Gaitonde, D., "Very High-Order Spatially Implicit Schemes for Computational Acoustics on Curvilinear Meshes", *J. Comp. Acoustics*, in press, 2001.

14. Thomas, P. and Lombard, C., "Geometric Conservation Law and its Application to Flow Computations on Moving Grids", *AIAA J.*, Vol. 17, No. 10, Oct. 1979.

15. Visbal, M. and Gordnier, R., "A High-Order Flow Solver for Deforming and Moving Meshes", AIAA Paper 2000-2619, June 2000.

16. Beam, R. and Warming, R., "An Implicit Factored Scheme for the Compressible Navier-Stokes Equations," *AIAA J.*, Vol. 16, No. 4, 1978.

17. Pulliam, T., "Artificial Dissipation Models for the Euler Equations", *AIAA J.*, Vol. 24, No. 12, Dec. 1986.

18. Pulliam, T. and Chaussee, D., "A Diagonal Form of an Implicit Approximate-Factorization Algorithm", *J. Comp. Phys.*, Vol. 39, No. 2, 1981.

19. Vichnevetsky, R., "Propagation Through Numerical Mesh Refinement for Hyperbolic Equations", *Math. and Comp. in Simulation*, XXIII, 1981.

20. Proceedings of the Second Computational Aeroacoustics (CAA) Workshop on Benchmark Problems. NASA Langley Research Center, Hampton, Virginia.

21. Visbal, M. and Gordnier, R., "Direct Numerical Simulation of the Interaction of a Boundary layer with a Flexible Panel", AIAA Paper 2001-2721, 2001.
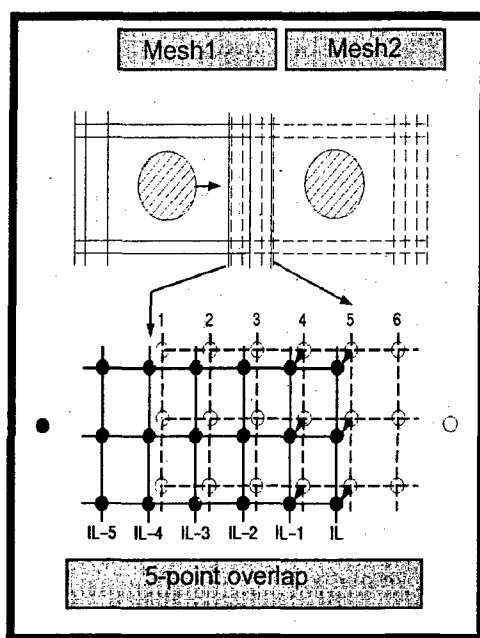
Fig. 1. Schematic of overlap strategy in high-order domain decomposition.
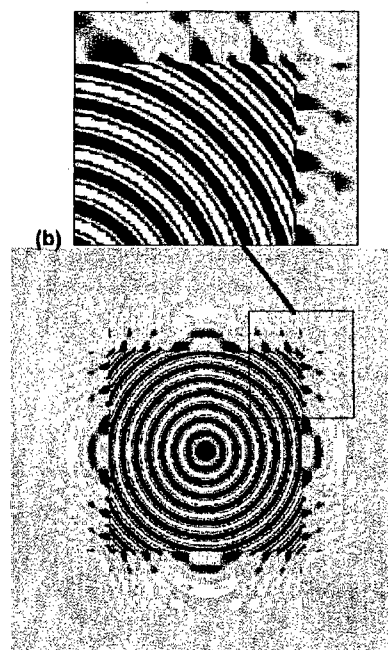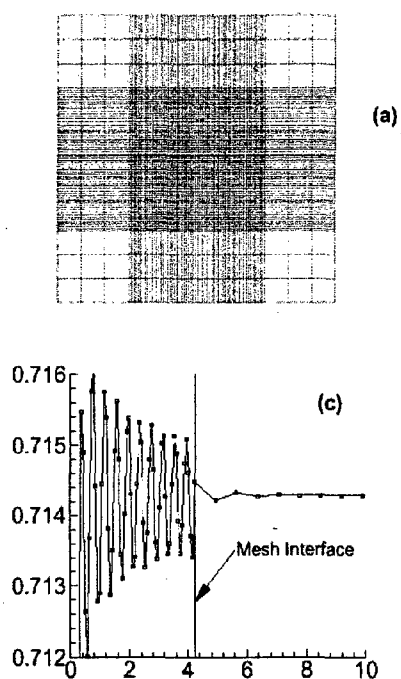

Fig. 2. Computation of 2-D acoustic source on mesh with abrupt stretching. (a) Grid, (b) Pressure contours, (c) Pressure along diagonal.
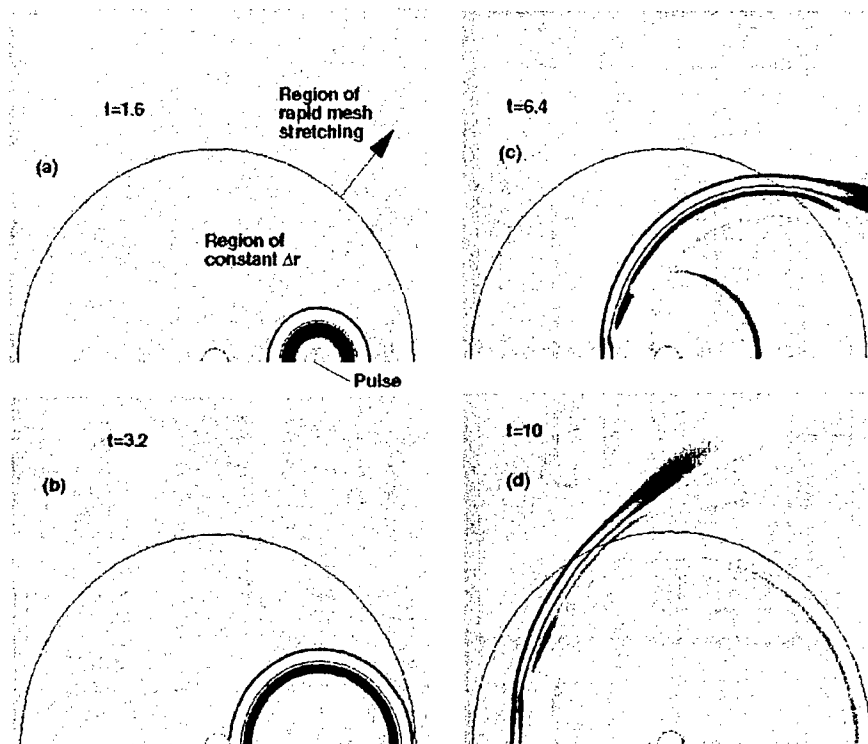
Fig. 3. Pressure contours at various instants for acoustic
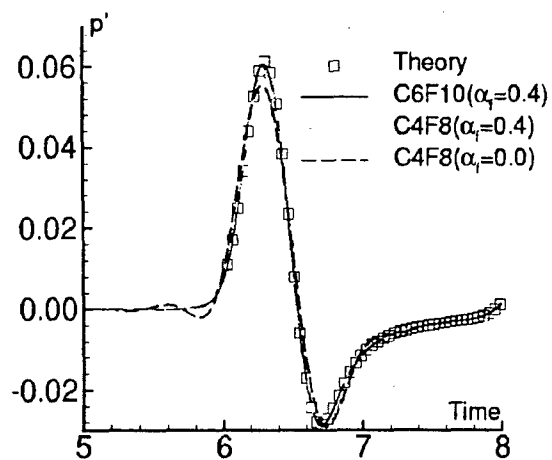pulse scattered by a circular cylinder.

Fig. 4. Computed pressure history at select
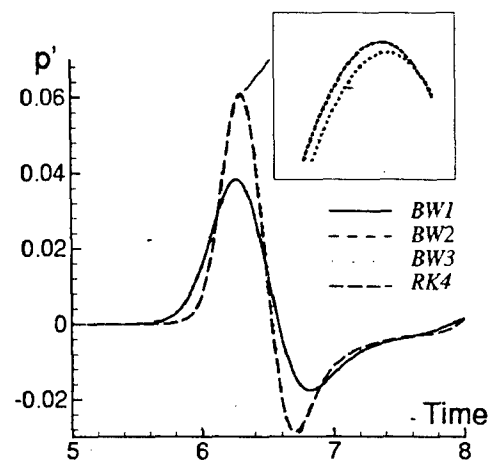point for several spatial discretizations and
the RK4 scheme.

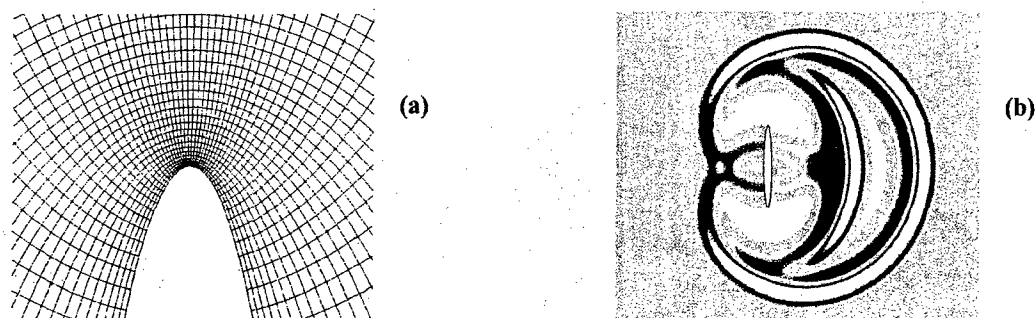Fig. 5. Comparison of implicit and
explicit time-marching schemes.

Fig. 6. Acoustic pulse scattered by elliptic cylinder. (a) Mesh , (b) Instantaneous pressure
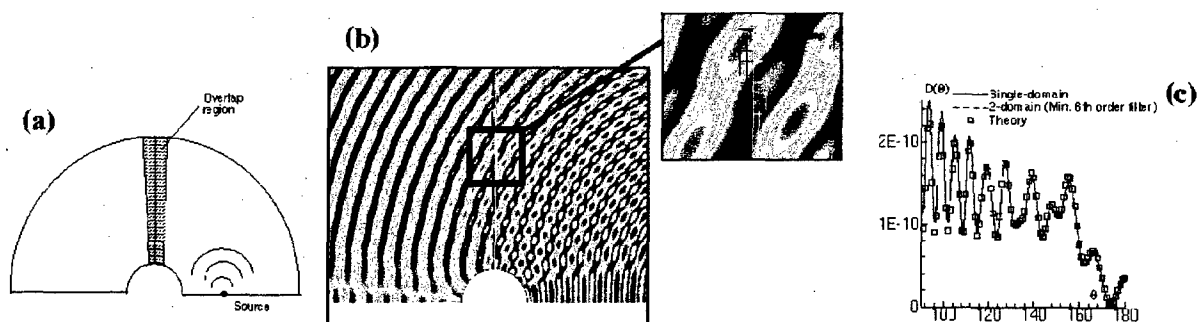contours at $t = 1.5$ for $C6F10$-$BW3$ scheme.

Fig. 7. Multi-domain scattering simulation. (a) Configuration, (b) pressure contours near mesh
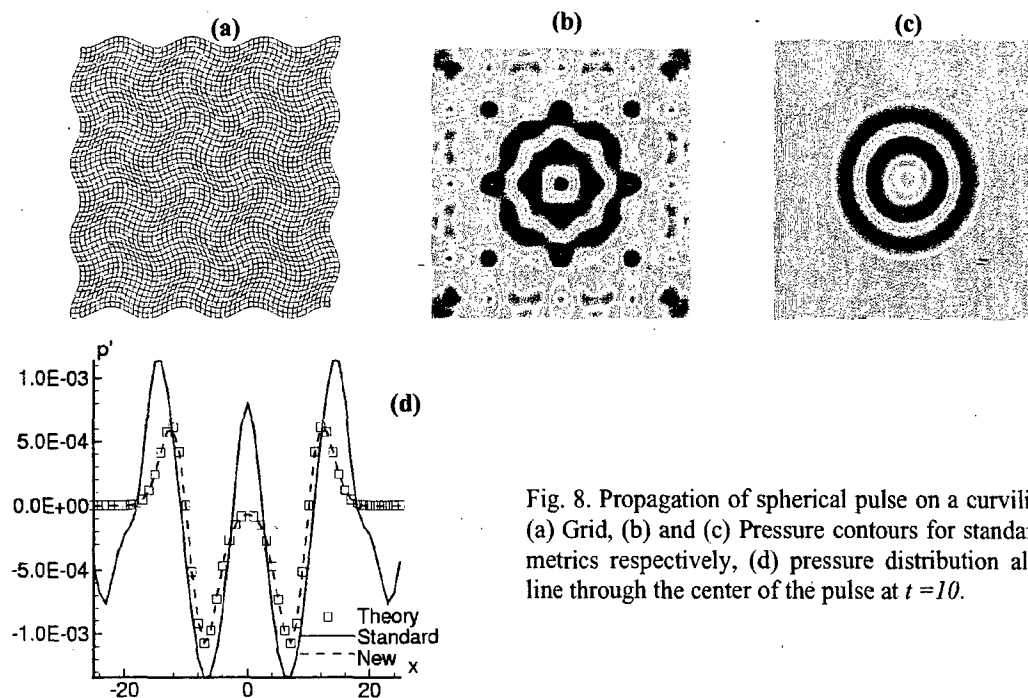overlap, (c) Directivity at $r/D = 5$.

Fig. 8. Propagation of spherical pulse on a curvilinear mesh.
(a) Grid, (b) and (c) Pressure contours for standard and new
metrics respectively, (d) pressure distribution along a grid
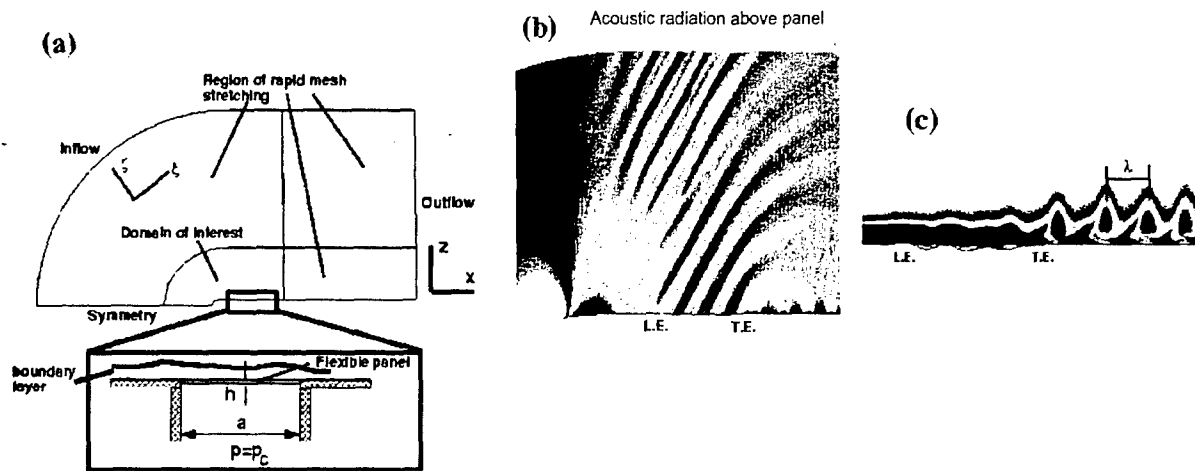line through the center of the pulse at $t =10$.

Fig. 9. Transitional boundary-layer flow over a fluttering elastic panel. (a) Configuration, (b) Instantaneous pressure, (c) Vorticity.